Effects of Initial Stress Field and Critical Slip-Weakening Distance on Rupture Selectivity of 3D Buried Branched Faults

Feng Qian[1] and Haiming Zhang[*1]

ABSTRACT

Using the boundary integral equation method with the slip-weakening friction law, we investigate the effects of the initial stress field and the critical slip-weakening distance on the rupture selectivity on the 3D buried branched faults. The numerical results show that after reaching the bifurcation line between the main fault and the branched faults, rupture continues to propagate on one or both bifurcation planes (BPs), with rupture on one plane more favorable than the other. The initial stress distribution plays a decisive role in the selection of the favorable BP (FBP), and there is a critical status of stress distribution, around which rupture propagates on both planes, whereas the FBP switches between the two. For a given fault geometry, the critical status of initial stress, which is described by a ratio *Fp* between normal stresses, is related to the critical slip-weakening distance D_c.

KEY POINTS

- We investigate what parameters affect the rupture selectivity of branched faults.
- We use a stress field and critical slip-weakening distance phase diagram to analyze branch fault selectivity.
- Rupture speed is critical in causing rupture of a branch that is less favorably oriented in the stress field.

Supplemental Material

INTRODUCTION

Fault branching phenomenon has been increasingly observed in natural fault systems with complex geometry, based on kinematic inversions and direct observation (Archuleta, 1984; Sowers *et al.*, 1994). It has an important impact on the rupture propagation directivity and the magnitudes of earthquakes. Therefore, studying the influence of fault branching on the rupture propagation and the key controlling factors on branched faults are important for understanding earthquake source processes. So far, numerical simulation of dynamic rupture has been applied to complex fault systems including fault branching (Oglesby *et al.*, 2003; Fukuyama and Mikumo, 2006; Ando *et al.*, 2017; Ando and Kaneko, 2018).

Dynamic spontaneous rupture depends on the stress state on the fault and is controlled by the friction criterion. For a branched fault in a uniform initial external tectonic stress field, the initial state of stress on each bifurcation plane (BP) can be analyzed by the Mohr's circle. The state of stress determines which BP is more prone to break (Aochi *et al.*, 2000, 2002; Kame *et al.*, 2003). In a dynamic rupture propagation, dynamic stress accumulation produced by previous ruptures affects the state of stress on the fault. Poliakov *et al.* (2002) studied the effect of the rupture velocity on the dynamic stress field at the rupture tip. When the rupture reaches the intersection with different propagation velocities, rupture propagation behaves differently (Kame *et al.*, 2003; Bhat *et al.*, 2004, 2007; Fliss *et al.*, 2005). The branching angle is the key factor describing the geometry of the branched fault. For a uniform tectonic stress field, different branching angles correspond to different initial stress states. On the other hand, because of the interaction between the BPs, the rupture propagating on one BP produces a stress reduction, which inhibits the rupture propagation on the other. This is usually called the "stress shadow effect" (Yamashita and Umeda, 1994). Undoubtedly, the branching angle is a key factor on the rupture interaction between the BPs (Aochi *et al.*, 2000; Kame *et al.*, 2003).

Because of the interaction between the BPs, in most cases the ruptures on branched faults choose to propagate only on one of the BPs after reaching the intersection and stop spreading on the other BP. The patterns of rupture on branched faults are highly influenced by the choice of BP. Numerical simulations of large earthquakes showed that fault branching plays an

1. Department of Geophysics, School of Earth and Space Sciences, Peking University, Beijing, China

*Corresponding author: zhanghm@pku.edu.cn

Cite this article as Qian, F., and H. Zhang (2020). Effects of Initial Stress Field and Critical Slip-Weakening Distance on Rupture Selectivity of 3D Buried Branched Faults, *Bull. Seismol. Soc. Am.* **110**, 816–824, doi: 10.1785/0120190255

important role in complex fault systems and affects the fault-plane geometry and magnitudes of earthquakes (Ando *et al.*, 2017; Ando and Kaneko, 2018). The state of stress on the fault plane determines the rupture behavior. For a given bifurcation angle, the initial state of stress determines which BP is more breakable, which can be analyzed using the Mohr's circle. However, when the rupture propagation is fast enough, the rupture propagates simultaneously on both BPs even if there is mutual inhibition (Kame *et al.*, 2003; Fliss *et al.*, 2005), because of the strong dynamic stress accumulation on the main fault plane.

In this study, we numerically simulate the spontaneous rupture on 3D branched faults by applying the boundary integral equation method (BIEM) with the slip-weakening law to investigate the behavior of rupture propagation on the BP. For the behavior of rupture propagation on the BP, we explore the influences of the initial stress and the slip-weakening distance on the rupture selectivity of branched faults. Although several studies have focused on the effects of the initial stress (Aochi and Fukuyama, 2002; Kame *et al.*, 2003; Duan and Oglesby, 2007; DeDontney *et al.*, 2012), most of them are based on 2D models and only specific stress field distributions are considered. More general and in-depth discussions on the influence of the initial stress are required. Actually, effects of 3D and finite thickness of fault play an important role in dynamic ruptures. The fault thickness has a decisive influence on the transition of crack-like to pulse-like, and will affect the propagation behavior of the rupture (Day, 1982). Critical slip-weakening distance is an important friction parameter in dynamic rupture simulations, and its value affects the behavior of rupture propagation, including the speed of rupture propagation and rupture energy radiation efficiency (Mikumo and Yagi, 2003; Tinti *et al.*, 2004; Fukuyama and Mikumo, 2007; Kaneko *et al.*, 2017). Here, we explore the influences of the initial stress field distribution and the critical slip-weakening distance on the 3D branched fault with finite thickness and a given bifurcation angle, and obtain a phase diagram to conveniently analyze the rupture selectivity. Because our focus is on the effect of geometry of branched fault, we did not consider the effect of free surface to avoid complex mixed effects. On the other hand, previous studies have shown that when the fault is located more than 1 km under the surface, the effect of free surface on rupture propagation becomes very small and can be neglected (Zhang and Chen, 2006). In this stage, we only consider buried faults on which the effect of free surface can be neglected.

NUMERICAL METHOD AND FAULT MODEL

We use the BIEM with an unstructured mesh (Qian *et al.*, 2019). The discretization form of BIEM as follows:

$$T_{mp} = T_m^0 + \sum_{n=1}^{N_X} \sum_{q=1}^{p} V_{nq} K_{mp/nq}, \tag{1}$$

in which T_{mp} is the stress of the element m at time p, T_m^0 is the initial stress, and V_{nq} is the slip rate of the element n at time q. The integration kernel $K_{mp/nq}$ is the stress Green's function (Feng and Zhang, 2017) in whole space, which represents the stress response between fault elements. The BIEM is used together with the slip-weakening friction law to obtain the slip rates and stresses on the fault elements. Given the fault geometry as well as the initial tectonic stress field and the friction parameters, the spatiotemporal evolution of the rupture process can be obtained.

The branched fault model that we consider in this study is shown in Figure 1a. The entire branched fault system consists of three planar faults: a main fault of dimension 30 km × 10 km and two bifurcated faults both of dimension 15 km × 10 km. Therefore, the fault has a finite thickness of 10 km. The minimum inscribed circle radius of the triangular elements $\Delta s = 249$ m. The medium parameters we used are set as follows. The P and S velocities are 5.6 and 3.2 km/s, respectively, the density is 3000 kg/m^3, and the timestep $\Delta t = 0.044$ s. Although the spatial grid size and timestep are not fine enough, they conform to the basic stability conditions. Because we are using BIEM, the current grid size is sufficient for the small D_c value. We verified this with some experiments in the supplemental material to this article. To initiate the rupture, we assumed that the initial shear stress in the nucleation zone, usually called "asperity," is slightly greater than the fault's peak strength (about 1.05 times). The rupture in inplane mode starts from a nucleation zone located on the main fault A and propagates outward. We set an unbreakable barrier at the edge of fault as the boundary condition. For the BIEM, there is no numerical singularity at the intersection node, only the stability conditions need to be satisfied, that is, no element will cross the intersection. When the rupture front reaches the intersection line, it selects one of the bifurcated faults (B or C) in most cases to continue according to different conditions.

As shown in Figure 1b, a uniform initial stress field is considered. The normal and shear stresses are assumed to be in z and x directions, respectively, and hence the slip is only along the x direction. The normal stress is compressive, that is, $-\sigma$, in which σ is the absolute value of the normal stress. Given the initial stress element on plane A σ_{zz}^A, σ_{xx}^A, and τ_{zx}^A, the maximum principal stress $S_{\max}$ can be determined, with Φ being the angle between plane A and the direction of the maximum principal stress. The initial stress field on planes B and C can be described by the normal stress $-\sigma_n$ and shear stress τ, which are related to the bifurcation angle φ. Kame *et al.* (2003) studied the 2D dynamic rupture for four specific values of Φ on branched faults and the results showed that different Φ-values may cause the rupture to propagate along different BPs. In this study, distribution of initial stress is investigated to find out how the initial stress field affects the rupture selectivity on the branched faults, and whether there is a critical stress field

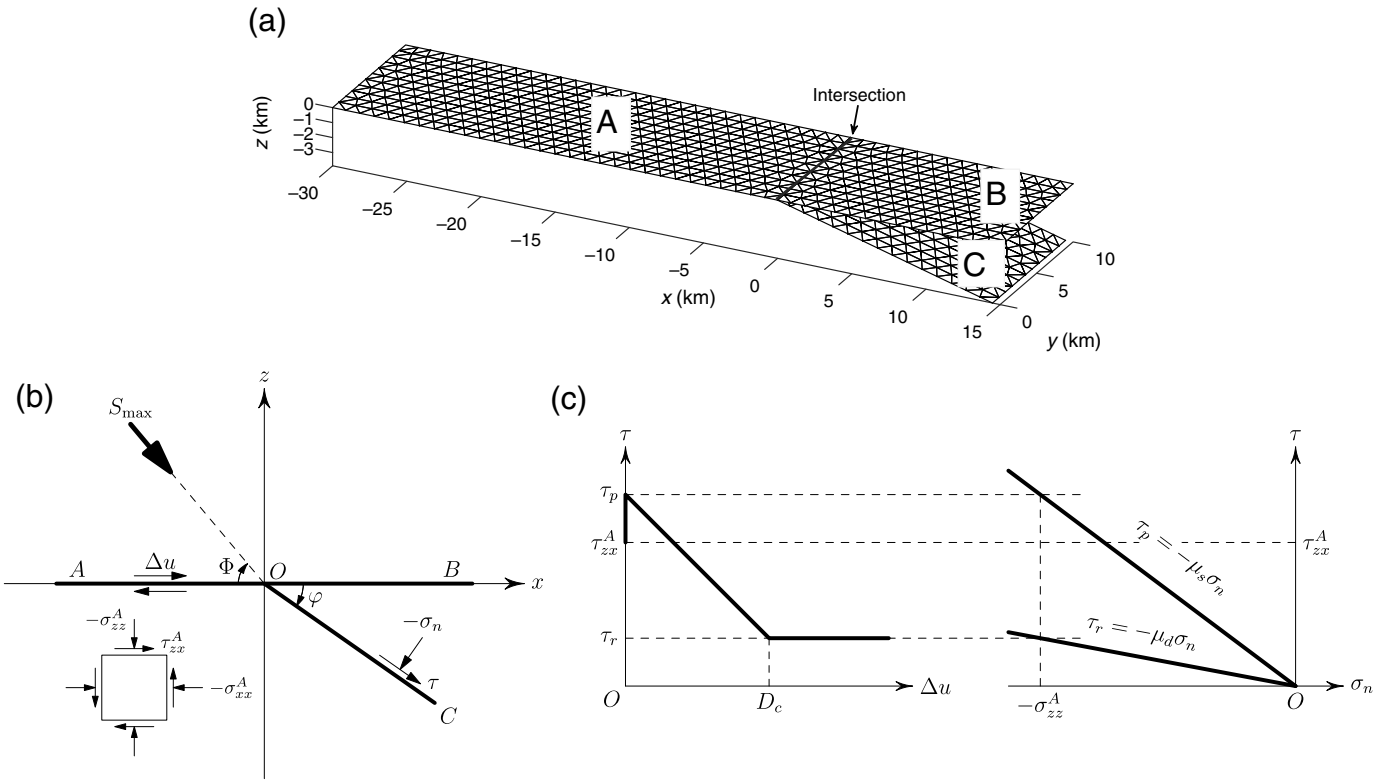

Figure 1. Model configuration and the slip-weakening friction law. (a) Configuration of the branched fault system considered in this study. The fault system consists of three fault planes: the main plane A and the bifurcated planes B and C. The angle between planes B and C is 15°. (b) Initial stress field. Black line indicates the branched fault system. τ and $-\sigma_n$ represent shear and compressive normal stresses on the fault planes, respectively. The thick black arrow shows the direction of the initial maximum principal stress $S_{\max}$. (c) Slip-weakening Coulomb friction law. The peak and residual shear stresses τ_p and τ_r are proportional to normal stress $-\sigma_n$.

distribution that causes the rupture to propagate on both BPs instead of propagating on only one of the BPs.

Fault rupture is controlled by the friction law. The slip-weakening law (Ida, 1972) is adopted to describe the relationship between strength and slip on the fault plane, as shown in Figure 1c. μ_d and μ_s are the dynamic and static friction coefficients, respectively, and their products with the normal stress are the residual strength and peak strength on the fault, respectively. D_c is the critical slip-weakening distance and is related to the rock property. In numerical simulations, to stabilize the propagation of the rupture, D_c is often related to the scale of the fault and the size of the unit (Fukuyama and Mizoguchi, 2010), which affects the rupture speed and the efficiency of energy radiation (Mikumo and Yagi, 2003; Tinti *et al.*, 2009). D_c is also an important factor responsible for the transition to super-shear rupture (Xu *et al.*, 2015). Uniform static and dynamic friction coefficients of $\mu_s = 0.6$ and $\mu_d = 0.1$ are assumed, which means that the fault has a high peak strength and a low residual strength. μ_s, μ_d, and D_c are distributed uniformly on the three faults A, B, and C, respectively. We change the value of D_c to explore its influence on the rupture propagation and selectivity of the BPs. A reference value of critical slip-weakening distance is defined as $D_0 = 0.57$ m.

NUMERICAL RESULTS

Rupture pattern on branched faults

For comparison, we consider three different fault models composed by the three fault planes A, B, and C in Figure 1, that is, a straight fault model with fault planes A and B, a bended fault model with fault planes A and C, and a branched fault model with all three fault planes A, B, and C. The final slip distributions for the three fault models are shown in Figure 2, and some snapshots are shown in Figures S1 and S2. In all three fault models, the rupture processes on the main fault plane A are indistinguishable. For the straight fault model, the rupture propagates continuously from fault A onto fault B (Fig. 2a and Fig. S1); whereas for the bended fault model, the rupture seems to pause temporarily at the intersection, and then propagates onto fault C with a different rupture speed and slip pattern (Fig. 2b and Fig. S2). For the branched fault model, when the rupture reaches the intersection, both faults B and C begin to rupture. However, the rupture on fault plane B soon ceases, whereas the rupture on fault C continues to propagate with a different rupture speed and shape of the rupture front. The addition of the bifurcated fault C causes the rupture behavior on fault B to change. The rupture on fault B is suppressed and the propagation is terminated.

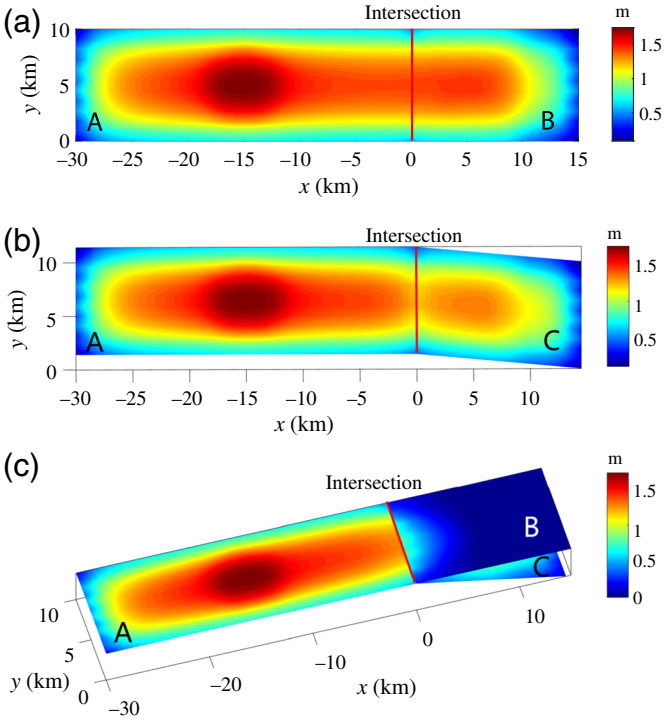

Figure 2. Final slip on the fault planes for fault models (a) with fault planes A and B, (b) with fault planes A and C, and (c) with fault planes A, B, and C. The color version of this figure is available only in the electronic edition.

Effect of the initial stress field

We use the ratio between the normal stresses to describe the initial stress field, defined as $Fp = (\sigma^A_{xx})/(\sigma^A_{zz})$. The value of Fp determines the angle Φ in Figure 1. We investigate the influence of the initial stress field on the rupture propagation with different values of Fp. The initial stress field on planes A is assumed as $\sigma^A_{zz} = 10$ MPa and $\tau^A_{zx} = 5$ MPa,, respectively. We change the value of Fp by changing σ^A_{xx} only so that the values of $-\sigma_n$ and τ on fault A do not change. This ensures that the rupture behavior on fault A does not change with Fp, which means that the rupture speed is always the same when it propagates to the intersection. Figure 3 shows the snapshots of slip distributions on the branched faults with different values of Fp. Because our focus is on the rupture selectivity of the branched fault, we did not compute the entire rupture process, the slip of last step is therefore not exactly the final (static) slip. It can clearly be seen that fault C is more favorable than fault B for rupture to continue for $Fp \leq 1.1$. After the rupture reaches the intersection, it almost always propagates onto fault C only, whereas on fault B the rupture is weak and only lasts for a very short period of time. On the other hand, fault B becomes more favorable for $Fp > 1.13$, when the rupture propagates almost always onto fault B only, whereas the rupture on fault C is much weaker. Kame *et al.* (2003) studied the branched fault and found that the initial stress field changes the selection of the favorable BP (FBP). In our results, we can also see that the FBP switches from fault plane C to B as Fp increases from 1.1 to 1.13. When $Fp \sim 1.13$, the rupture propagates on both fault planes B and C, which is consistent with the Kame *et al.* results on the rupture behavior and selectivity.

Effect of the critical slip-weakening distance

We also investigate how the critical slip-weakening distance D_c affects the rupture propagation on bifurcation faults. Figure 4 shows the snapshots of the slip rate with different D_c in the range of $[0.76D_0, 1.24D_0]$ and a fixed $Fp = 1.1$. The rupture propagates on both BPs as $D_c \leq 0.88D_0$. In this case, fault B is more favorable with a larger slip rate but a smaller rupture speed than fault C. Previous studies (Fukuyama *et al.*, 2003; Tinti *et al.*, 2004) have shown that D_c affects the rupture and width of the rupture front. The overall rupture width is determined by the time delay between the leading rupture front and the trailing healing front, whereas D_c mainly affects the rupture behavior (the high slip-rate part) near the leading rupture front and the fault thickness could influence of the arrival time of the healing front. Smaller values of D_c result in larger rupture intensity and smaller rupture width, which is consistent with our results. Kame *et al.* (2003) studied the effect of rupture speed on the rupture propagation along the branched faults. It has also been found that when the rupture speed is high, the rupture usually propagates on both BPs. When D_c is in the range of $[0.92D_0, 1.04D_0]$, the rupture still propagates on both BPs, but fault C is more favorable, and the rupture on fault B becomes weaker with increasing D_c. For $D_c > 1.08D_0$, the rupture propagates on both BPs again, with larger energy partitioned to fault B and at a higher rupture speed while both slip and slip rate are smaller on fault C. As D_c increases, the rupture speed becomes faster and the rupture front grows wider. For large D_c, the rupture front is thicker, and when its edge reaches the intersection, initiates a relatively weak rupture on fault C. On the other hand, the rupture on fault B is triggered by the main energy of the rupture front, which accumulates more energy. Meanwhile, the rupture on fault C has expanded over a certain distance, causing a smaller restraining effect on fault B, such that the rupture on fault B is able to propagate with more energy.

Phase diagram for rupture selectivity

Because both the initial stress field and the critical slip-weakening distance D_c influence the rupture selectivity of the branched faults, we perform a total of 50×50 simulations of the rupture processes in the parameter space (D_c, Fp), and obtain the rupture phase diagram. Figure 5a shows the FBP for given parameters (D_c, Fp), in which the FBP is defined by the ratio of the maximum slip between faults C and B. It clearly shows that the FBP is fault B for large Fp but fault C for small Fp. There is a transition zone of Fp, in which the rupture continues to

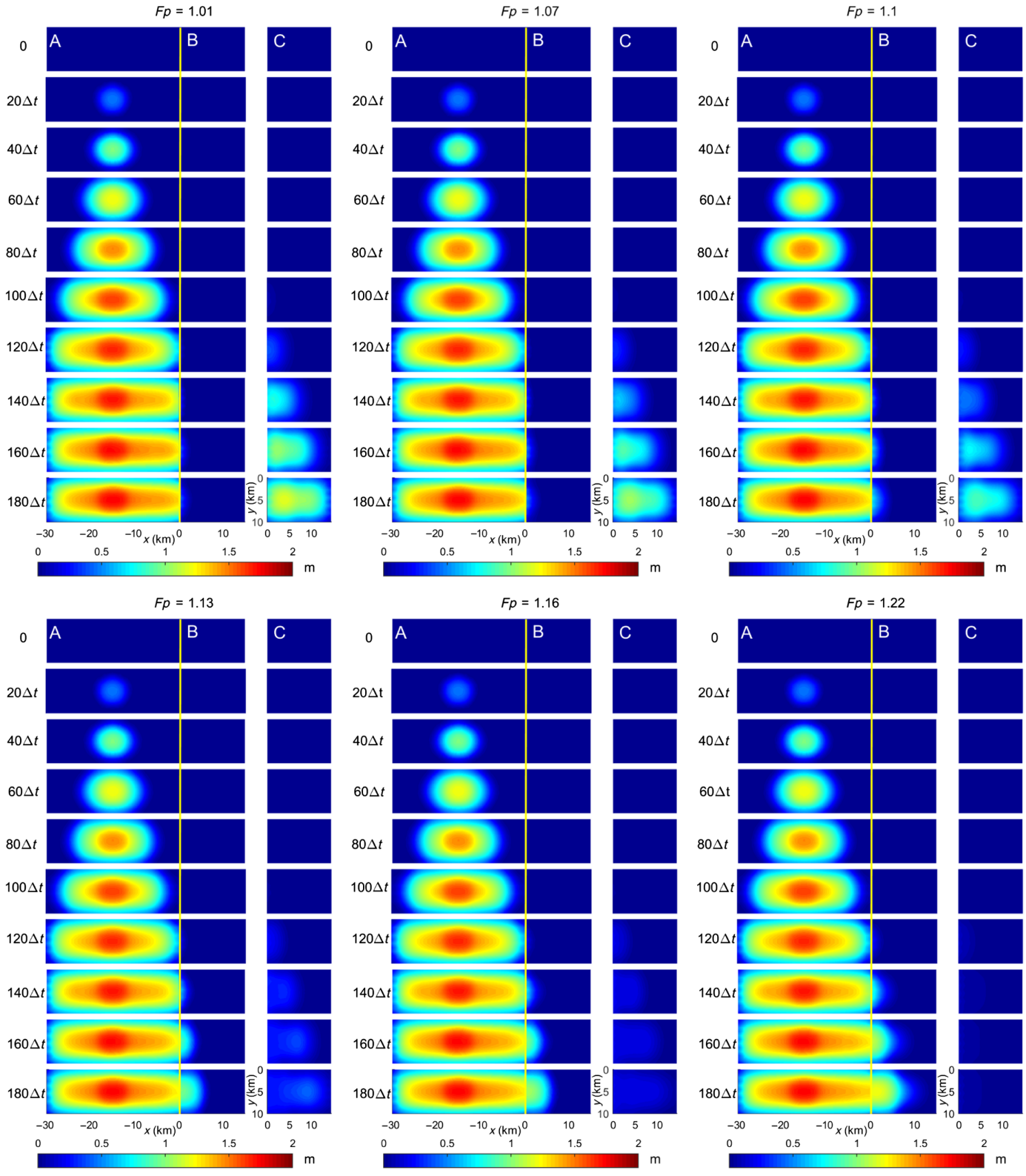

propagate on both BPs, and the FBP switches between them. The critical value of Fp is related to D_c. When $D_c \in (0.64D_0, 1.0D_0)$, the critical value of Fp increases linearly with D_c. However, the critical value of Fp decreases linearly with D_c, for $D_c \in (1.0D_0, 1.3D_0)$.

Figure 3. Snapshots of accumulated slip distribution on the branched faults with different values of the normal stress ratio Fp. Yellow lines depict the intersection. In all cases, $D_c = D_0$. The color version of this figure is available only in the electronic edition.

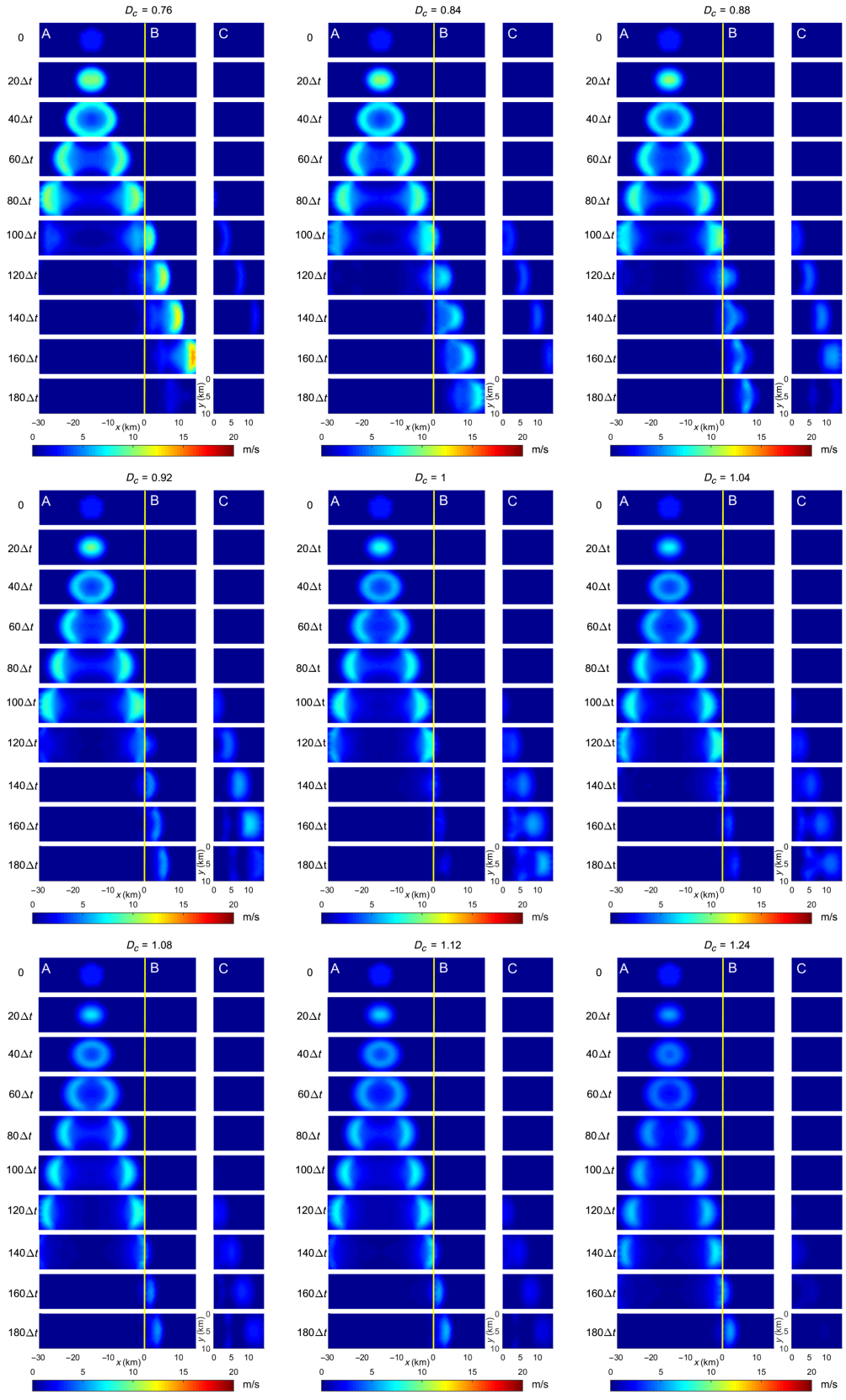

Figure 4. Snapshots of slip-rate distribution for different values of the critical slip-weakening distance D_c. The color version of this figure is available only in the electronic edition.

DISCUSSIONS

Initial stress field on BPs

The initial stress field on the BP can be analyzed by the Mohr's circle, as shown in Figure 5c. Given the initial stress field *Fp*, the angle between the maximum principal stress direction and the main fault plane A is determined, and point B corresponds to the stress state on planes A and B. The stress state on plane C is represented by point C on the Mohr's circle with the angle between points B and C being 2φ. The slopes of the two dotted lines through the origin correspond to the dynamic and static friction coefficients, respectively, and the rupture is able to propagate only when the stress status is located in the area between the two dotted lines. It can be inferred from the slip-weakening criterion that the closer the stress state is to the static friction line, the easier it is for the rupture to propagate, and vice versa. Andrews (1976) defined the following parameter to characterize the propagation ability of the rupture:

$$S = \frac{\tau_p - \tau_0}{\tau_0 - \tau_r}, \qquad (2)$$

in which τ_p and τ_r are the peak and residual strengths, respectively, and τ_0 is the initial shear stress. The smaller the *S*-value is, the easier it is for rupture propagation. It is obvious that the vertical distance from a point on the Mohr's circle to the upper dotted line is $\tau_p - \tau_0$, and the vertical distance to the lower dotted line is $\tau_0 - \tau_r$. With the change of *Fp*, the angle 2Φ changes accordingly, and we can calculate the relative change of *S* for points B and C. When *Fp* is small, Φ is large, and point

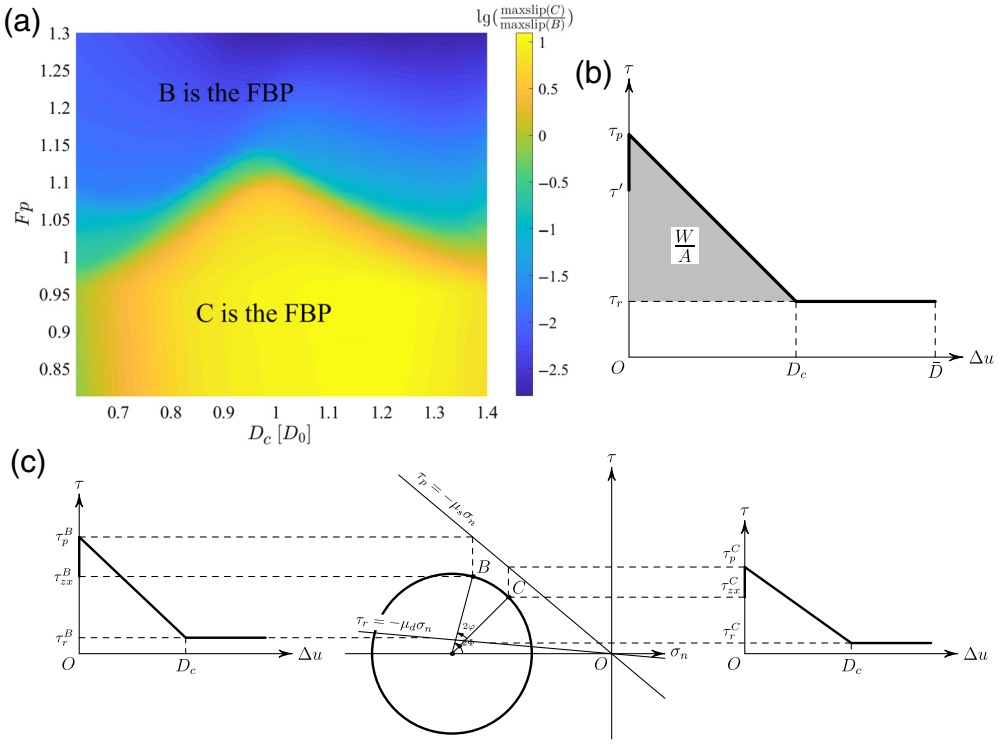

Figure 5. (a) Phase diagram of the branched fault selectivity. D_c is the critical slip-weakening distance. *Fp* is the normal stress ratio of the initial stress field. Colorbar corresponds to the logarithm of the ratio of the maximum slip between faults B and C. (b) Rupture fracture energy under the slip-weakening friction law. *W* and *A* are the fracture energy and area, respectively. (c) Mohr's circle. Points B and C on the Mohr's circle represent the initial stress state of fault B and C, respectively. ⍰ is the angle between fault plane B and the direction of the maximum principle stress, and φ is the angle between faults B and C. The color version of this figure is available only in the electronic edition.

C is closer to the upper dotted line, indicating a smaller *S*-value and an easier rupture state on fault C. In contrast, when *Fp* is large, Φ is small, and point B is closer to the upper dotted line, indicating a smaller *S*-value and an easier rupture state on fault B. When *Fp* is near some special value so that the *S*-values for points B and C are very close, the rupture can propagate on both bifurcated faults.

D_c and rupture energy distribution

Figure 5b is a rupture propagation energy distribution diagram under the slip-weakening law. The fracture energy required for rupture is proportional to D_c. When D_c is small, the fracture energy required for rupture propagation is low, and the propagation efficiency of rupture is high. The rupture speed and the slip rate are also high, which is consistent with the results shown in Figure 4. For larger rupture speed, Kame *et al.* (2003) also found that ruptures are more likely to propagate on both BPs, which is consistent with our results for small D_c. From the analysis of Mohr's circle, it is easy to see that fault C is in an easier rupture state when $Fp = 1$. When D_c is small, the rupture on fault C propagates fast with a narrow rupture front, accumulating only a little energy. However, fault B accumulates more energy and ruptures soon after fault C ruptures.

Interaction between BPs

Figure 2 reveals that there is a mutual inhibition between the BPs of the branched faults. The slip on one BP generates negative stress accumulation on the other, thereby preventing the rupture from being generated, due to the so-called "stress shadow effect" (Yamashita and Umeda, 1994). In BIEM, the stress accumulation is the convolution between the stress Green's function and the slip rate. Figure 6 shows the comparison of the stress Green's functions between different points on different faults. It is obvious that *Kab* and *Kac* can produce stress accumulation, while *Kbc* leads to the stress reduction, which confirms the mutual inhibition between the BPs of the branched faults.

CONCLUSIONS

We use numerical simulations based on the BIEM to investigate the effect of the initial stress field and the critical slip-weakening distance D_c on the selection of the FBP during the rupture propagation process for a 3D branched fault model, and obtained the phase diagram for the selection of the FBP. An important feature of the branched faults is the mutual inhibition between the BPs, such that the rupture propagates on only one of the BPs in most cases, or on both BPs but one has more dominant energy than the other. Through the analysis of Mohr's circle, we find that the initial stress field determines the rupture propagation ability parameter *S* on the BP, which controls the selection of the FBP. There exists a critical value for the ratio of normal stresses *Fp* in the initial stress field. When *Fp* is near the critical value, both the BPs rupture, whereas the rupture propagates only on the FBP when *Fp* is away from the critical value. When *Fp* changes across the critical value, the FBP switches from one of the BPs to the other. The phase diagram shows that the value of the critical *Fp* is related to the slip-weakening distance D_c. When D_c is smaller, the rupture speed is larger, and it is easier for the two fault planes to rupture together, with a more dominant energy on the bifurcation fault parallel to the main fault. When D_c is larger, due to the influence of the rupture front width, although one BP with a smaller *S* ruptures first, it contains

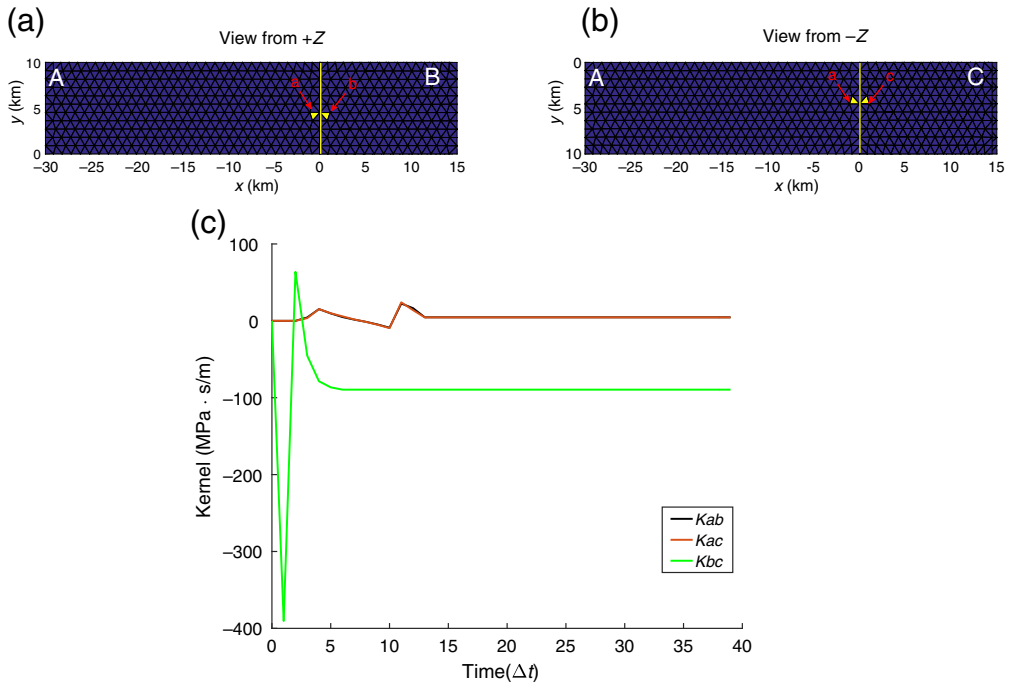

Figure 6. Comparison of stress Green's functions. (a) Looking from the top down showing elements a and b on faults A and B, respectively. (b) Looking from the bottom up showing elements a and c on faults A and C, respectively. (c) Comparison of kernels *Kab*, *Kac*, and *Kbc*, in which *Kij* is the stress Green's function for elements *i* and *j* ($i, j = a, b, c$, and $i \neq j$). The color version of this figure is available only in the electronic edition.

little energy, whereas the BP with a larger *S* accumulates stress for a longer period of time to propagate with greater energy.

DATA AND RESOURCES

Numerical data used for generating figures and movies in this article are open at https://opendata.pku.edu.cn/dataverse/zhanghm (last accessed February 2020). Supplemental material contains more details about the snapshots of some numerical results.

ACKNOWLEDGMENTS

This study is supported in part by the National Natural Science Foundation of China (Grant 41874047) and by the High-performance Computing Platform of Peking University. The authors acknowledge the course "English Composition for Geophysical Research" of Peking University for help in improving this article. The authors express their deep gratitude to Associate Editor Delphine D. Fitzenz and two anonymous reviewers for their thoughtful comments and detailed suggestions to improve the article.

REFERENCES

Ando, R., and Y. Kaneko (2018). Dynamic rupture simulation reproduces spontaneous multifault rupture and arrest during the 2016 M_w 7.9 Kaikoura earthquake, *Geophys. Res. Lett.* **45,** no. 23, 12,875–12,883, doi: 10.1029/2018gl080550.

Ando, R., K. Imanishi, Y. Panayotopoulos, and T. Kobayashi (2017). Dynamic rupture propagation on geometrically complex fault with along-strike variation of fault maturity: Insights from the 2014 Northern Nagano earthquake, *Earth Planets Space* **69,** doi: 10.1186/s40623-017-0715-2.

Andrews, D. J. (1976). Rupture velocity of plane strain shear cracks, *J. Geophys. Res.* **81,** no. 32, 5679–5687.

Aochi, H., and E. Fukuyama (2002). Three-dimensional nonplanar simulation of the 1992 Landers earthquake, *J. Geophys. Res.* **107,** no. B2, ESE 4-1–ESE 4-12, doi: 10.1029/2000JB000061.

Aochi, H., E. Fukuyama, and M. Matsu'ura (2000). Selectivity of spontaneous rupture propagation on a branched fault, *Geophys. Res. Lett.* **27,** no. 22, 3635–3638, doi: 10.1029/2000gl011560.

Aochi, H., R. Madariaga, and E. Fukuyama (2002). Effect of normal stress during rupture propagation along nonplanar faults, *J. Geophys. Res.* **107,** no. B2, doi: 10.1029/2001jb000500.

Archuleta, R. J. (1984). A faulting model for the 1979 imperial-valley earthquake, *J. Geophys. Res.* **89,** no. B6, 4559–4585.

Bhat, H. S., R. Dmowska, J. R. Rice, and N. Kame (2004). Dynamic slip transfer from the Denali to Totschunda faults, Alaska: Testing theory for fault branching, *Bull. Seismol. Soc. Am.* **94,** 202–213.

Bhat, H. S., M. Olives, R. Dmowska, and J. R. Rice (2007). Role of fault branches in earthquake rupture dynamics, *J. Geophys. Res.* **112,** no. B11, doi: 10.1029/2007jb005027.

Day, S. M. (1982). Three-dimensional finite difference simulation of fault dynamics: Rectangular faults with fixed rupture velocity, *Bull. Seismol. Soc. Am.* **72,** no. 3, 705–727.

DeDontney, N., J. R. Rice, and R. Dmowska (2012). Finite element modeling of branched ruptures including off-fault plasticity, *Bull. Seismol. Soc. Am.* **102,** no. 2, 541–562, doi: 10.1785/0120110134.

Duan, B., and D. D. Oglesby (2007). Nonuniform prestress from prior earthquakes and the effect on dynamics of branched fault systems, *J. Geophys. Res.* **112,** no. B5, doi: 10.1029/2006jb004443.

Feng, X., and H. M. Zhang (2017). Equivalent formulae of stress Green's functions for a constant slip rate on a triangular fault, *Earthq. Sci.* **30,** no. 3, 115–123, doi: 10.1007/s11589-017-0186-3.

Fliss, S., H. S. Bhat, R. Dmowska, and J. R. Rice (2005). Fault branching and rupture directivity, *J. Geophys. Res.* **110,** no. B6, doi: 10.1029/2004jb003368.

Fukuyama, E., and T. Mikumo (2006). Dynamic rupture propagation during the 1891 Nobi, central Japan, earthquake: A possible extension to the branched faults, *Bull. Seismol. Soc. Am.* **96,** no. 4, 1257–1266.

Fukuyama, E., and T. Mikumo (2007). Slip-weakening distance estimated at near-fault stations, *Geophys. Res. Lett.* **34,** no. 9, doi: 10.1029/2006gl029203.

Fukuyama, E., and K. Mizoguchi (2010). Constitutive parameters for earthquake rupture dynamics based on high-velocity friction tests with variable sliprate, *Int. J. Fract.* **163,** nos. 1/2, 15–26.

Fukuyama, E., T. Mikumo, and K. B. Olsen (2003). Estimation of the critical slip-weakening distance: Theoretical background, *Bull. Seismol. Soc. Am.* **93,** no. 4, 1835–1840.

Ida, Y. (1972). Cohesive force across the tip of a longitudinal-shear crack and Griffith's specific surface energy, *J. Geophys. Res. Atmos.* **77,** no. 20, 3796–3805, doi: 10.1029/JB077i020p03796.

Kame, N., J. R. Rice, and R. Dmowska (2003). Effects of pre-stress state and rupture velocity on dynamic fault branching, *J. Geophys. Res.* **108,** no. B5, 1–19.

Kaneko, Y., E. Fukuyama, and I. J. Hamling (2017). Slip-weakening distance and energy budget inferred from near-fault ground deformation during the 2016 M_W 7.8 Kaikōura earthquake, *Geophys. Res. Lett.* **44,** no. 10, 4765–4773, doi: 10.1002/2017gl073681.

Mikumo, T., and Y. Yagi (2003). Slip-weakening distance in dynamic rupture of inslab normal-faulting earthquakes, *Geophys. J. Int.* **155,** no. 2, 443–455, doi: 10.1046/j.1365-246X.2003.02047.x.

Oglesby, D. D., S. M. Day, Y. G. Li, and J. E. Vidale (2003). The 1999 Hector Mine earthquake: The dynamics of a branched fault system, *Bull. Seismol. Soc. Am.* **93,** no. 6, 2459–2476, doi: 10.1785/0120030026.

Poliakov, A. N. B., R. Dmowska, and J. R. Rice (2002). Dynamic shear rupture interactions with fault bends and off-axis secondary faulting, *J. Geophys. Res.* **107,** no. B11, doi: 10.1029/2001jb000572.

Qian, F., B. Wu, X. Feng, and H. Zhang (2019). 3D numerical simulation of dynamic ruptures on complex fault systems by BIEM with unstructured meshes, *Chin. J. Geophys.* **62,** no. 9, doi: 10.6038/cjg2019M0642.

Sowers, J. M., J. R. Unruh, W. R. Lettis, and T. D. Rubin (1994). Relationship of the Kickapoo fault to the Johnson Valley and Homestead Valley faults, San Bernardino County, California, *Bull. Seismol. Soc. Am.* **84,** no. 3, 528–536.

Tinti, E., A. Bizzarri, A. Piatanesi, and M. Cocco (2004). Estimates of slip weakening distance for different dynamic rupture models, *Geophys. Res. Lett.* **31,** no. 2, doi: 10.1029/2003gl018811.

Tinti, E., M. Cocco, E. Fukuyama, and A. Piatanesi (2009). Dependence of slip weakening distance (D_c) on final slip during dynamic rupture of earthquakes, *Geophys. J. Int.* **177,** no. 3, 1205–1220, doi: 10.1111/j.1365-246X.2009.04143.x.

Xu, J. K., H. M. Zhang, and X. F. Chen (2015). Rupture phase diagrams for a planar fault in 3-D full-space and half-space, *Geophys. J. Int.* **202,** no. 3, 2194–2206.

Yamashita, T., and Y. Umeda (1994). Earthquake rupture complexity due to dynamic nucleation and interaction of subsidiary faults, *Pure Appl. Geophys.* **143,** nos. 1/3, 89–116.

Zhang, H., and X. Chen (2006). Dynamic rupture on a planar fault in three-dimensional half-space—II. Validations and numerical experiments, *Geophys. J. Int.* **167,** no. 2, 917–932, doi: 10.1111/j.1365-246X.2006.03102.x.

Manuscript received 10 October 2019
Published online 10 March 2020